Atomically resolved EELS mapping of the interfacial structure of epitaxially strained $LaNiO_3/LaAlO_3$ superlattices

N. Gauquelin,[1,*] E. Benckiser,[2,†] M. K. Kinyanjui,[3] M. Wu,[2] Y. Lu,[2] G. Christiani,[2] G. Logvenov,[2] H.-U. Habermeier,[2] U. Kaiser,[3] B. Keimer,[2] and G. A. Botton[1,‡]

[1]*Department of Materials Science and Engineering and Canadian Centre For Electron Microscopy, McMaster University, 1280 Main Street West, Hamilton, Ontario, Canada L8S 4M1*

[2]*Max Planck Institute for Solid State Research, Heisenbergstr. 1, 70569 Stuttgart, Germany*

[3]*University of Ulm, Central Facility of Electron Microscopy, Albert-Einstein Allee 11, 89081 Ulm, Germany*

(Received 2 July 2014; revised manuscript received 4 November 2014; published 20 November 2014)

The interfacial atomic structure of a metallic $LaNiO_3/LaAlO_3$ superlattice grown on a $LaSrAlO_4$ substrate was investigated using a combination of atomically resolved electron energy loss spectroscopy (EELS) at the Al K, Al $L_{2,3}$, Sr $L_{2,3}$, Ni $L_{2,3}$, La $M_{4,5}$, and O K edges as well as hybridization mapping of selected features of the O K-edge fine structure. We observe an additional $La_{1-x}Sr_xAl_{1-y}Ni_yO_3$ layer at the substrate-superlattice interface, possibly linked to diffusion of Al and Sr into the growing film or a surface reconstruction due to Sr segregation. The roughness of the $LaNiO_3/LaAlO_3$ interfaces is found to be on average around one pseudocubic unit cell. The O K-edge EELS spectra revealed reduced spectral weight of the prepeak derived from Ni-O hybridized states in the $LaNiO_3$ layers. We rule out oxygen nonstoichiometry of the $LaNiO_3$ layers and discuss changes in the Ni-O hybridization due to heterostructuring as possible origin.

DOI: 10.1103/PhysRevB.90.195140 PACS number(s): 79.20.Uv, 68.37.−d, 68.35.Ct, 73.20.−r

I. INTRODUCTION

The quest for an atomic-level understanding of physical and chemical phenomena such as superconductivity and ionic transport have increased the need for experimental probes with very high spatial and energy resolution [1]. Aberration-corrected electron microscopy is a key tool for understanding the properties of materials as it provides a means by which the electronic and atomic structure can be investigated at subangstrom resolution. This is especially valuable in the investigation of ultrathin oxide superstructures. In recent years, considerable research effort has been directed to epitaxially strained superstructures [2–6] as it has been shown that epitaxial strain can be used to modulate orbital occupation leading to novel electronic properties [5,7–9]. Specifically, extensive research activity has focused on $LaNiO_3$ (LNO) based heterostructures, initiated by theoretical work which predicted a structural/electronic nickelate analog of high-temperature cuprate superconductors [10–13]. In bulk LNO, the nickel atoms are octahedrally coordinated to six oxygen atoms, leading to an O_h symmetry and partially degenerate $3d$ orbitals, i.e., lower-lying threefold-degenerate t_{2g} and higher-lying twofold-degenerate e_g levels. The nominal electron configuration of the Ni ions is $t_{2g}^6 e_g^1$, however, due to the strong hybridization of the Ni d orbitals with the p orbitals of the ligand oxygen ions, Ni^{3+} may be more properly understood as $Ni^{2+}\underline{L}$, where $\underline{L}$ denotes a ligand hole in the oxygen p states [14–16].

Density functional theory has addressed the influence of confinement, strain, structural distortions, chemical composition of the insulating layers, and electronic correlations on the electronic structure of LNO based superlattices, with widely divergent results [11–13,17–20]. A recent comparative study based on local density approximation plus dynamical mean-field theory has shed light on the partially contradictory results of previous calculations [21], which showed that the effect of electronic correlations enhance or reduce the effective crystal field, depending on whether the less correlated p orbitals are included or not. In calculations with a basis set including only the most important correlated d orbitals close to the Fermi level, a significant orbital polarization of the Ni d state was found and discussed to possibly give rise to a Fermi surface akin to those of the copper-oxide high-temperature superconductors [11]. In contrast, when the oxygen p orbitals are explicitly included in the calculations by choosing a large basis [19], the Ni ground state is largely composed of Ni $3d^8\underline{L}$. For realistic e_g splittings, in this electron configuration each e_g orbital, i.e., the x^2-y^2 and the $3z^2-r^2$ orbital, is occupied by one electron due to Hund's coupling, rendering the system robust against orbital polarization. In experiments, so far, a lifting of the degeneracy of the e_g levels for thin films of LNO grown on compressive-strain-inducing substrates was reported from x-ray linear dichroism [9,22]. Qualitatively similar results were observed for a $LNO/LaAlO_3$ (LAO) superlattice grown under compressive strain from a combined study of soft x-ray linear dichroism and reflectometry [23]. In the latter study, the spatially resolved orbital polarizations within the 4-unit-cell-thick layer stacks of LNO were determined. In particular, the two inner LNO layers, which are exempt from any influence from the interface and predominantly affected by the compressive strain show a preferred occupation of the e_g $3z^2-r^2$ orbital and a splitting of the e_g levels around 100 meV [23]. Unveiling the origin of orbital polarization requires a deeper understanding of the underlying structural and electronic properties of nickel oxides, in particular a more detailed knowledge about the hybridization strength of nickel and oxygen in these heterostructures. This information can be obtained from the pre-edge region of the oxygen K-edge

*Current Address: EMAT, Department of Physics, University of Antwerp, Groenenborgerlaan 171, 2020 Antwerp, Belgium; Nicolas.Gauquelin@uantwerpen.be

†E.Benckiser@fkf.mpg.de

‡Corresponding author: gbotton@mcmaster.ca

spectrum. However, to study possible differences in the Ni-O hybridization within a 4-pseudo-cubic-unit-cell-thick LNO layer stack in a LNO/LAO superlattice, this information is required in a spatially resolved manner.

Here, we report element-specific, spectrally resolved maps obtained by aberration-corrected scanning transmission electron microscopy–energy loss near-edge structure (STEM–ELNES). In order to study the roughness and atomic arrangement, a local probe such as STEM is required and EELS is, to date, the only method which allows us to study changes in electronic structure at interfaces from one atomic column to the next. We focus on the results of a LNO/LAO superlattice grown under compressive strain induced by a $LaSrAlO_4$ substrate and discuss in detail the results of both types of interfaces, namely, the substrate-superlattice interface (Sec. IV A) and the interfaces between LNO and LAO within the superlattice (Sec. IV B).

II. EXPERIMENTAL DETAILS

A LNO/LAO superlattice with stacking sequence of (4u.c./4u.c.)×10 pseudocubic unit cells (u.c.) was epitaxially grown on a [001]-oriented $LaSrAlO_4$ (LSAO) substrate by pulsed laser deposition as described in detail in Ref. [23]. The stacking sequence started with the first LNO layer and one encapsulating LAO layer finished the growth for protection of the underlying LNO layer. TEM samples were prepared using an NVision 40 dual-beam focused ion beam system (Carl Zeiss AG, Germany) equipped with a 30-kV Ga^+ ion gun. Prior to the focused ion beam (FIB) process a 20-nm-thick gold layer was deposited on the surface of the whole sample for protection. As a first step of the FIB sample preparation, a 20-nm-thick layer of W was *e*-beam deposited on the surface for further protection of the surface of the sample. This *e*-beam deposition decreases the damage of the sample as electrons rather than the usual gallium ions (which have a higher-energy transfer) are used to deposit W on the surface of the sample prior to FIB milling. The sample was thinned down to a relative thickness of $t/\lambda = 1.4$ (where t is the absolute thickness and λ is the inelastic mean-free path of the electrons in the TEM at the selected accelerating voltage of 200 keV and estimated to 77 nm using the parametrization of Malis *et al.*) [24] using progressively decreasing ion beam energies in the FIB down to 1 keV. This process was followed by Ar^+ milling with 900-eV ions at liquid nitrogen temperature using a Fischione Model 1040 NanoMill® until a thickness of around $t/\lambda = 0.25$ was reached, i.e., approximately 14 nm according to Malis *et al.* [24]. The localized milling area obtained using this instrument helps reduce damage of the sample during thinning as shown in our previous work [15,25]. A similarly prepared FIB TEM lamella of a thick film of LNO (100 nm) grown under the same conditions as the superlattice was used as a reference for pure $LaNiO_3$ in order to discuss the stoichiometry and electronic structure of the PLD grown film. Scanning transmission electron microscopy (STEM) measurements were performed for imaging with high-angle annular dark-field (HAADF) and electron energy loss spectroscopy (EELS) on an FEI Titan 80-300 Cubed® TEM (FEI Company, Eindhoven, The Netherlands) equipped with a high-brightness electron source, aberration correctors for probe and image lenses, a monochromator, and a high-resolution electron energy loss spectrometer Gatan Tridiem®.

The experiments were performed at 200 kV in STEM mode where a fine probe of about 1 Å was rastered on the specimen. From each pixel, the high-angle scattered electrons were collected using an HAADF detector while an EEL spectrum was recorded using the spectrometer. Dispersion and exposure time of 0.5 eV–0.1 s/pixel for atomic mapping of high-energy edges (Al K and Sr L) and 0.2 eV–0.03 s/pixel for the mapping of the O K, La M, and Ni L edges were used. A collection angle larger than 100 mrad can be achieved in energy-filtered STEM (EFSTEM) mode, allowing practically all the scattered electrons in the EELS entrance aperture, and a convergence semiangle of 20 mrad was used to record the EELS data. The O K edge is extracted from the EELS spectrum by a standard power-law background subtraction [26]. In order to reduce the noise in the data, some spectral images, as specified where appropriate in the text, were processed using the multivariate weighted principal component analysis routine (PCA) (MSA Plugin in Digital Micrograph®) developed by M. Watanabe [27]. Special care was taken that this PCA treatment did not alter the contrast distribution seen in the raw data. Further separation of the overlapping La $M_{4,5}$ and Ni $L_{2,3}$ edges was realized using the multiple linear least square fitting (MLLS). MLLS fitting can be applied to map spatially both edges independently using internal reference spectra for La (from the substrate) and Ni (by subtraction of the reference La spectra in the LNO layers). Possible beam damage during measurement will be discussed in detail further in the following. The spectral imaging data sets were acquired in monochromated mode, thus improving the energy resolution from around 1 to 0.17 eV. For the high-energy resolution data, the spectra were acquired with 0.05 eV/pixel dispersion and acquisition times of 1 s/pixel. The hybridization maps called Ni 3d, La 5d, Sr 4d, Al 3p in Fig. 5 were obtained by integrating the background-subtracted intensity in the energy windows: [528-531], [532-536.5], [537-539], and [542.5-545], respectively, corresponding to the energy range of the hybridized bands between the O 2p electrons with the corresponding bands of the cations. The O_h and D_{4h} components shown in Fig. 7 are extracted in the same way from regions in energy [528-529.5] and [529.5-531], respectively. HAADF multislice image simulations were performed using the QSTEM software package [28]. Sample thickness used for simulation was 70 nm in the angular range 70–200 mrad.

The dc resistance measurements were performed in van der Pauw geometry using a home-built four-probe setup with liquid helium cooling. For this purpose, four droplike contacts were made with conducting silver paint in the corners of the 5×5 mm^2 large samples, which were subsequently studied by STEM-ELNES. The resistivity was calculated by $[\pi/\ln(2)] * R(T) * d$ where $R(T)$ is the measured resistance and d is the total thickness of the conducting LNO layer stacks (total thickness determined from x-ray diffraction divided by two).

III. RESULTS

A. Elemental EELS mapping

Bulk LNO and LAO exhibit rhombohedral room-temperature structures (space group $R\bar{3}c$). Starting from the

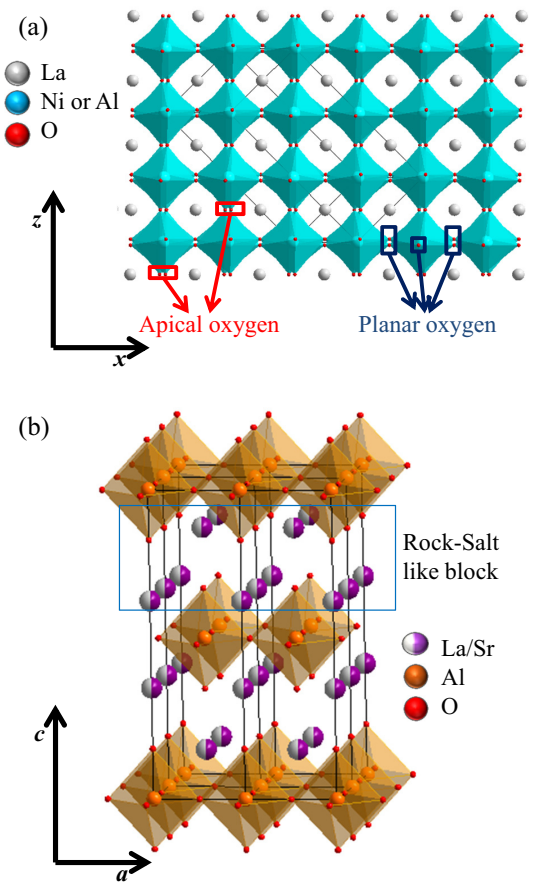

FIG. 1. (Color online) Crystallographic structures of (a) $LaMO_3$ (M = Ni, Al) and (b) $LaSrAlO_4$.

cubic perovskite, the structure can be described by cooperative rotations of the octahedra about the cubic [111] direction. When displayed in the rhombohedral $[\bar{2}20\bar{1}]$ direction, the pseudocubic unit cell is easily visible in Fig. 1(a) with the cell axes parallel to the z and x directions. LSAO crystallizes in the K_2NiF_4 Ruddlesden-Popper structure (space group $I4/mmm$) which consists of an alternating stacking of (La,Sr)O rock-salt-type layers and (La,Sr)AlO_3 perovskite building blocks with no octahedral tilts along the c (z) direction as shown in Fig. 1(b). Compressive strain from the LSAO substrate and heterostructuring with LAO influences the tilt pattern of the octahedra within the LNO layer stacks [29], and in turn can also affect the electronic structure by changing the proportions of metallic, covalent, and ionic parts to the chemical bonding [30].

Figures 2(a) and 2(b) present atomically resolved STEM-HAADF images of a segment of the superstructure obtained when imaging down the [100] zone axis. The intensity in the HAADF image is dominated by La/Sr columns followed by Ni atoms and Al atoms. O atomic columns are, on the other hand, nearly undetected in HAADF due to their low atomic number. LNO layers appear brighter than LAO layers due to their higher average Z number.

Two kinds of interfaces within the heterostructure can be recognized: the (reconstructed) LSAO/(first LNO) interface [substrate-overlayer interface, lines (I) and (II) in Fig. 2(b)]

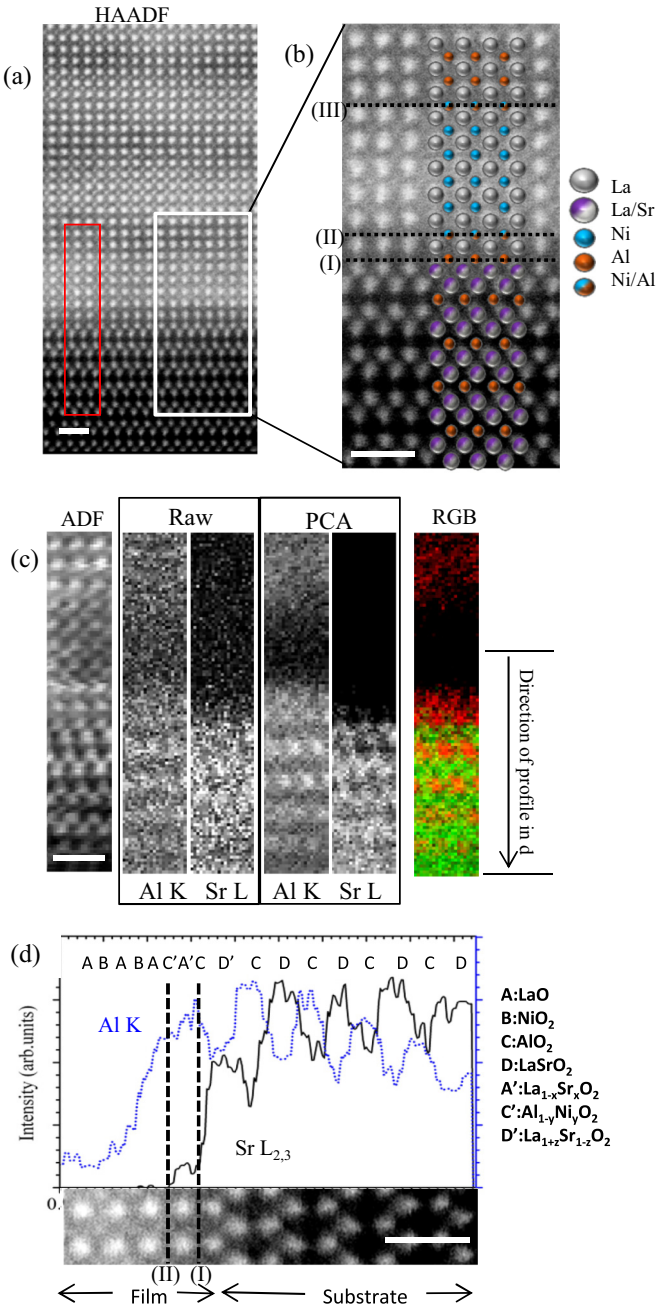

FIG. 2. (Color online) (a) HAADF image of the substrate and the first few LNO/LAO blocks. The red box outlines the location of the EELS maps displayed in (c). (b) Magnification of the interface with structural overlap. (c) Nonprocessed (raw panel) and PCA-processed EELS atomic maps of Al and Sr. A RGB composite map of the Al K edge (red) and Sr L edge (green) is displayed on the right panel of (c). (d) Intensity profiles from Al (blue curve) and Sr (black curve) spectrum images generated by summing the spectra line by line along the profile showed in panel (c). A reproduction of the HAADF image is shown in order to determine the stacking sequence as explained in the text. Scale bars are in units of 1 nm.

and the LNO/LAO interfaces [superlattice interfaces; line (III) in Fig. 2(b)].

Using the maps of Sr $L_{2,3}$ (1940 and 2007 eV) and Al K (1560 eV) as well as the HAADF intensity as a reference

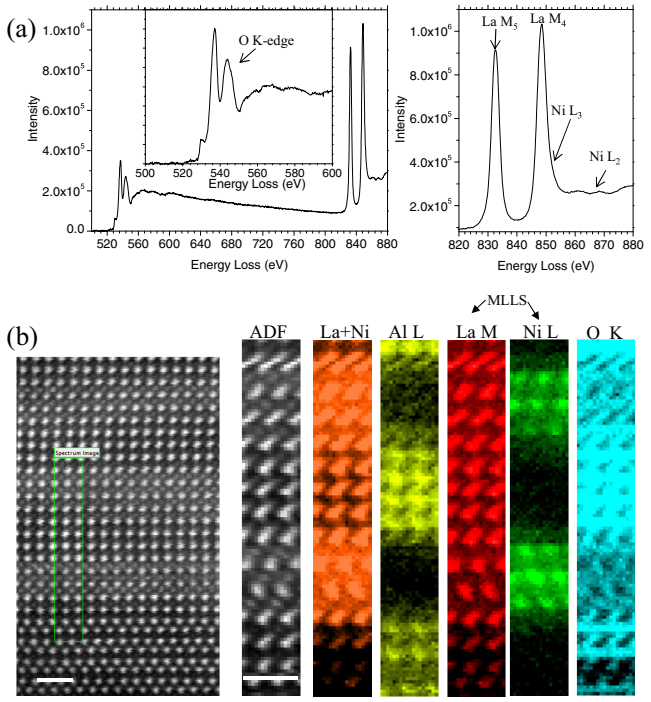

FIG. 3. (Color online) (a) Integrated electron energy loss spectrum in the LNO region with La $M_{4,5}$, Ni $L_{2,3}$, and O K edges. (b) Atomically resolved maps showing the overlapping La-Ni map (orange), the Al L-edge map (yellow), the MLLS extracted contributions of La M edge (red) and Ni L edge (green), and finally the total O K edge (PCA treated). Scale bars are in units of 1 nm.

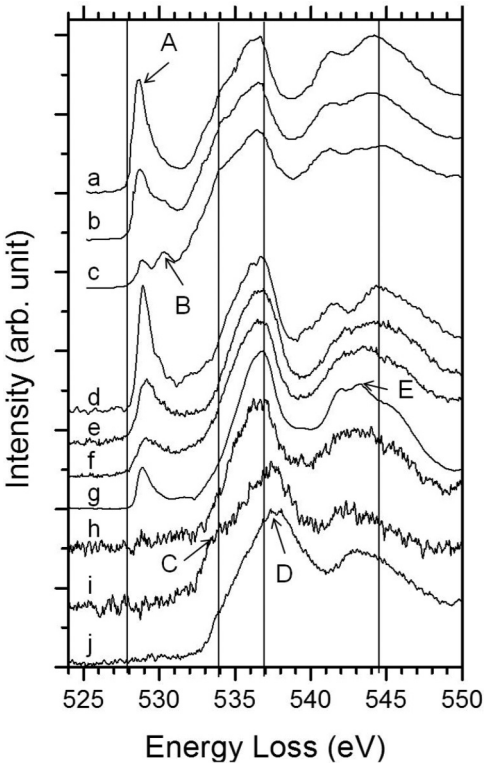

FIG. 4. Comparison between literature XAS for different stoichiometries of $LaNiO_{3-x}$ [$LaNiO_3$ (a), $LaNiO_{2.75}$ (b), and $LaNiO_{2.57}$ (c)]. Reprinted with permission from Abbate *et al.* [32] [Copyright (2002) by the American Physical Society]. Raw monochromated EELS spectra of the thick film (bulk), a LNO layer in the superlattice, and the entire superlattice (integrated over the entire spectrum image) in d, e, and f, respectively. Spectrum g shows the experimental raw XAS measurement. The bottom spectra are from the bulk $LaSrAlO_4$ substrate i, the topmost $(La,Sr)AlO_4$ layer of the substrate j, and the topmost LAO superlattice layer at the surface of the sample h. The different regions used for hybridization mapping are marked and described in the text with labels A to E.

for the La atomic column positions, the atomic stacking sequence is $LaSrO_2$-AlO_2-$La_{1+z}Sr_{1-z}O_2$-AlO_2-$La_{1-x}Sr_xO$-$Al_{1-y}Ni_yO_2$-LaO-NiO_2, where x, y, and z represent cationic defects due to incomplete layers and roughness [Figs. 2(c) and 2(d)]. We note the presence of a supplementary LAO layer on top of the substrate [its interface to the first LNO layer stack is marked by line (II) in Fig. 2(b)]. Note that the Al map presented in Fig. 2(d) was obtained using the Al $L_{2,3}$ edge at ~73 eV and this map is not as clear as the one from Fig. 2(b) presenting the Al K edge due to the larger delocalization of inelastically scattered electrons at lower energies as reported by several authors and reviewed in Ref. [31].

The atomically resolved EELS maps [Fig. 3(b)] confirm the atomic arrangement determined from the HAADF images. Since the La M_4 and Ni L_3 edges strongly overlap in energy [Fig. 3(a)], it difficult to unambiguously extract and map the Ni L-edge contribution. However, using the MLLS approach (see the Experimental Details section), we were able to extract maps of La, Ni, Al, and O [Fig. 3(b)] revealing an atomic stacking sequence across the interfaces (I), (II), and (III) which is in good agreement with the results presented in Fig. 2(c). The diffuse Al intensity distribution in the Al L map in Fig. 3(b) combined with the lower intensity in the Ni L map again suggests a partial mixing of Al and Ni at interfaces (II) and (III). To further investigate this roughness of around one unit cell at the superlattice interfaces, we carried out measurements using the bonding hybridization revealed from the ELNES of the O K edge.

B. Band hybridization mapping

The fine structure of the O K edge can be extracted from a high-energy resolution measurement as shown in Fig. 4. The O K edge onset in LAO is around 532 eV, whereas in LNO a strong prepeak can be identified around 528.5 eV (peak labeled A). This prepeak can be related to the transition from O 1s core levels to O 2p final states hybridized with Ni 3d states where Ni atoms are in the Ni^{3+} formal valence and in the O_h symmetry [32]. In nonstoichiometric $LaNiO_{3-\delta}$, the formation of vacancies on the apical oxygen (see Fig. 1, z direction) has been reported [33,34], giving rise to a D_{4h} symmetry at Ni and changing its nominal oxidation state from Ni^{3+} to Ni^{2+}. X-ray absorption studies have connected the appearance of a second prepeak around 530.5 eV (peak labeled B) with such changes in the local crystal field [32]. The peak at 536.5 eV is related to La 5d–O 2p hybridized states. The spectrum of bulk LSAO [spectrum (i) in Fig. 4] presents a strong feature around 533.5 eV (peak C), which is related to the strong La-O interaction in the rock-salt layer of the Ruddlesden-Popper structure [15,35]. Spectral regions (D) and (E) correspond to O

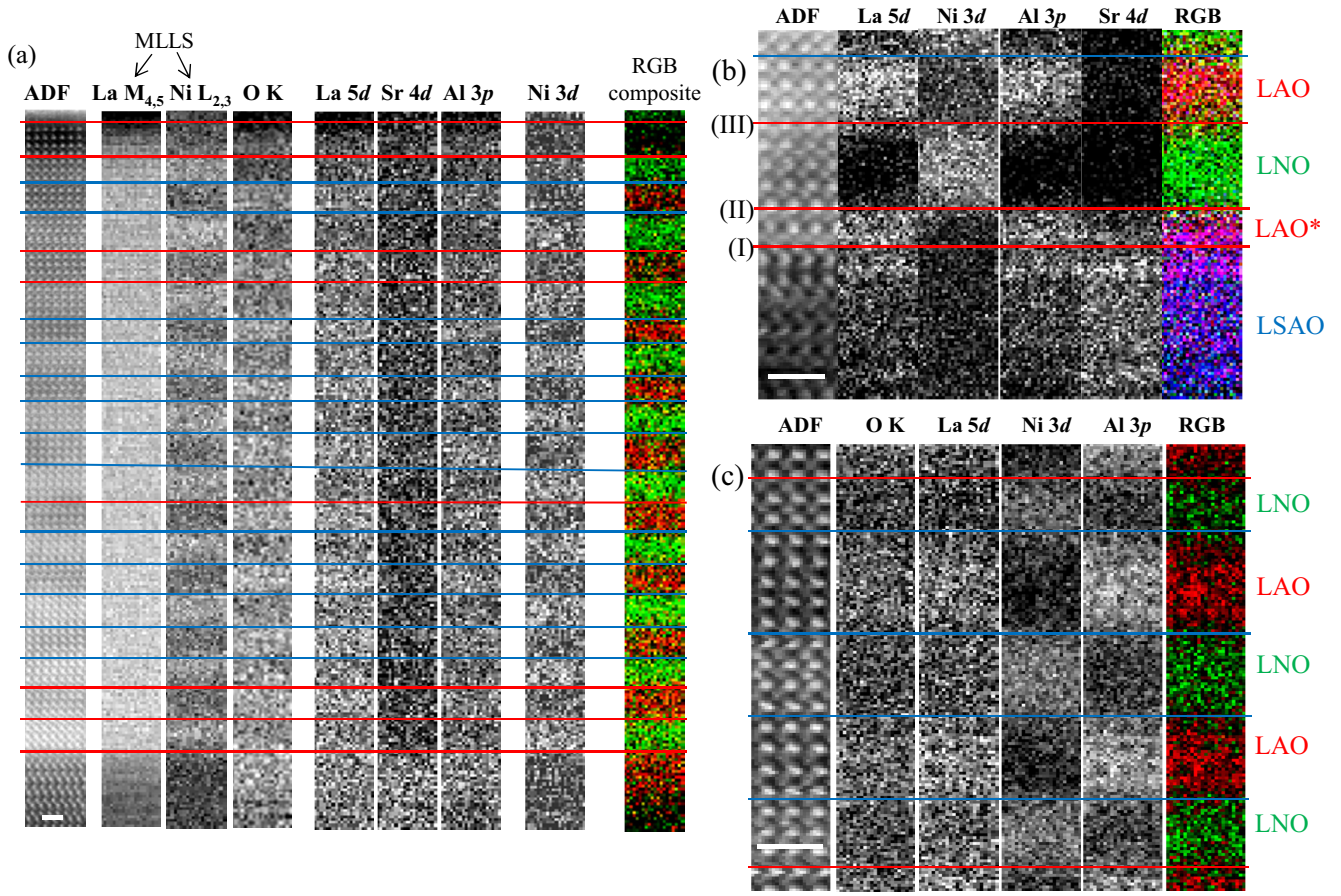

FIG. 5. (Color online) (a) Atomically resolved maps of La, Ni, and O full edges, along with hybridization maps of the 4//4×10 u.c. superlattice. The hybridization mapping is done using the energy ranges of the O K edge as outlined in Fig. 4 (raw data without application of the PCA, apart from the RGB composite). (b) Hybridization mapping of the (reconstructed) substrate-overlayer interface (I and II) and the first two superlattice interfaces. (c) Hybridization mapping of a few LNO/LAO superlattice interfaces. Two interfaces can be distinguished, which either have a LaO atomic interfacial layer (marked with red lines) or are of (Al, Ni)O_2 atomic composition (marked with blue lines). For RGB composites, the following color code was used: red: Al 3p–O 2p; green: Ni 3d–O 2p; and blue: Sr 4d–O 2p. Scale bars are in units of 1 nm.

2p states hybridized with Sr 4d and Al 3p states, respectively. The states within the energy range corresponding to peak (E) are not only due to O 2p states hybridized with Al 3p states but as well to Ni 4sp and Sr 5p states.

The spatial variation of the intensity in the energy windows corresponding to peaks A–E allows us to determine the distribution of these bands within the sample (Fig. 5). Figure 5(a) shows EELS elemental maps extracted from a spectrum image, as well as hybridization maps for the complete superlattice, including a few monolayers of the substrate. At first sight, we observe the strong correlation between the La-M and Ni-L elemental maps with the La 5d and Ni 3d hybridization maps, respectively. The total oxygen signal shows higher intensities in the LAO regions. The reconstruction at the substrate-overlayer interface, i.e., the presence of a LAO block [marked with an asterisk in Fig. 5(b)] at the surface of the substrate and discussed in the previous section based on the Al L-edge maps, is consistent with the lower intensity in the Sr 4d–O 2p map and the stronger intensity in the Al 3p–O 2p and La 5d–O 2p band hybridization map. Changes within the region 542–545 eV will not be further discussed in this work as this energy range is related to highly delocalized Sr, Al, and Ni related states making it irrelevant for attributing these contributions to a particular species.

From the maps corresponding to the hybrid states at the O K edge, the interface (III) between the first LNO layer and the first LAO* layer also appears to be sharp on the local scale of the measurement consistently with the element maps of Fig. 2. The termination of the first LNO layer is therefore a LaO atomic layer [marked by a red line in Fig. 5(b)] in this specific region. In contrast, the interface of the second LAO layer and the next LNO layer on top appears rather diffuse [blue line in Fig. 5(b)] and oxygen atoms at the interface are hybridized with both Al and Ni, suggesting the presence of a mixed (Al,Ni)O_2 interfacial atomic layer.

IV. DISCUSSION

A. Substrate-overlayer interface

The top $LaSrO_2$ atomic layer of the substrate $LaSrAlO_4$ is Sr depleted as shown on Fig. 2 whereas a small amount is present in the first LaO atomic layer of the film. This can be interpreted in two different ways: (1) the segregated Sr terminal layer of the substrate might form carbonate or hydroxide phases which

may be removed upon heating the substrate to 730 °C during the sample growth. (2) Diffusion of Al and Sr into the first LNO layer of the growing film may happen in the early stage of the PLD deposition.

The segregation of SrO at the surface of the substrate, predicted by Becerra-Toledo [36] and leading to a reconstruction of the subsurface area to the thermodynamically favored LAO phase, can be hypothesized. A subtle difference between the Al $3p$–O $2p$ hybridization map (Fig. 5) and the Al K (Fig. 2) and Al L (Fig. 3) elemental maps at the interface can be noticed: a stronger intensity can be noticed within this interface perovskite LAO block at the surface of the substrate than in the rest of the bulk LSAO [Fig. 5(c)]. This effect demonstrates that, locally, there is a change in the oxygen environment due to the compositional change with respect to the rest of the substrate.

In fact, the strong feature around 533.5 eV (peak C in Fig. 5), reflecting the strong La-O interaction in the rock-salt layer of the Ruddlesden-Popper structure of LSAO as shown previously for $La_{n+1}Ni_nO_{3n+1}$ [15], is not present in the first layer of the substrate (spectrum h in Fig. 4). This highlights a change of the oxygen environment suggested by the hybridization maps from Fig. 5. The shift of the major peak in the surface layer of LSAO can thus be related to the difference in bonding between Al-O in LAO and LSAO. This may occur as a result of difference in the second coordination shell of the oxygen atoms and/or octahedral tilts in LAO. The analysis of the HAADF images together with multislice simulations revealed that this interfacial layer is indeed not pure but a $Al_{1-x}Ni_xO_2$ mixed layer (Fig. 6).

Thereafter, two different scenarios can be hypothesized explaining the reconstruction of this interface. (i) Nondiffusive scenario: the substrate is assumed to be AlO_2 terminated and the first atomic layer that grows on top is a LaO layer, together forming one perovskite unit cell of $LaAlO_3$. Then, atomic layers of NiO_2, LaO, . . . follow. Note that this model excludes any interdiffusion of Al from the substrate and deposited Ni during growth. (ii) Diffusive scenario: the substrate is $La_{1-x}Sr_xO$ terminated (surface cleaved between the two $La_{0.5}Sr_{0.5}O$ layers) and the first atomic layer that bond to the substrate surface is NiO_2. In this scenario, the experimentally observed interface structure [Fig. 2(b)] indicates diffusion of Al inside the growing LNO film from the substrate.

B. LNO/LAO interfaces within the superlattice

From our EELS and HAADF measurements (shown further in Fig. 12 and discussed in details in Ref. [37]), we conclude that the LNO/LAO interface roughness is around 1 unit cell (u.c.) and each layer stack has an average thickness of 4 u.c. in good agreement with the results from x-ray reflectivity [8,23].

In comparing the intensity of the oxygen K-edge Ni $3d$ prepeak between experimental EELS data collected in each of the 10 layers stacks of $LaNiO_3$ to the reference data, we notice a non-negligible difference in intensity. A further decomposition of this prepeak into two bands can be accomplished by selecting two different energy regions corresponding to Peaks A and B in Fig. 4 to map the O_h and D_{4h} components. This decomposition is not possible in two-dimensional maps but more readily visible in intensity profiles integrated over the

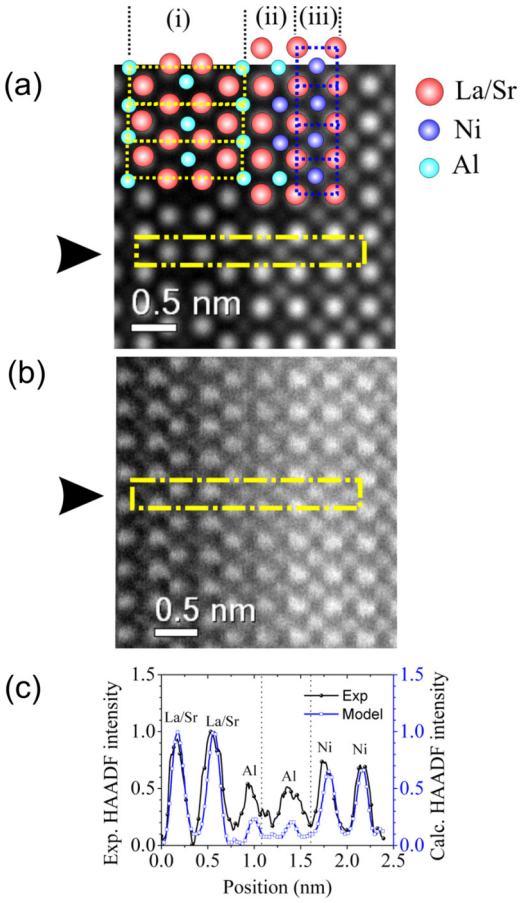

FIG. 6. (Color online) (a) Experimental HAADF image of the $LaSrAlO_4$/LNO interface. (b) Calculated HAADF image and atomic model of the interface. (c) Intensity profiles obtained along the yellow line marked by arrows in calculated and experimental images. The dotted rectangle marks the interfacial layer.

all-spectrum image along the layers (perpendicular to the z direction) for statistical noise reduction. Figure 7 shows the contributions to these hybridization levels and relative variations within the layer stacks and reveals that the O_h component is decreasing in the two topmost LNO layer stacks whereas the D_{4h} contribution is rather constant. It is important to note that this is not quantitative as we neglect the weight of the tail of the O_h contribution in the D_{4h} energy range as within the experimental resolution no clear separation can be made between the O_h and D_{4h} peaks shown in Ref. [32]. We argue that this is related to a change of the Ni-O bonding in these layers and can be interpreted by a reduction of Ni^{3+} to Ni^{2+} near the surface or the presence of vacancies and surface relaxation at the apical oxygen positions forcing the Ni^{3+} into a square-planar configuration.

The quantitative analysis of the prepeak contribution at 529 eV for the lower-lying LNO layer stacks reveals a ∼25% lower intensity compared to the thick LNO film grown on the same substrate and under the same conditions. We can further notice the presence of a non-negligible prepeak to the oxygen K edge within the superlattice stack in each LAO layer which should not be present in the LAO layer as shown for the LAO10 spectra in Fig. 8. These two phenomena might be intimately

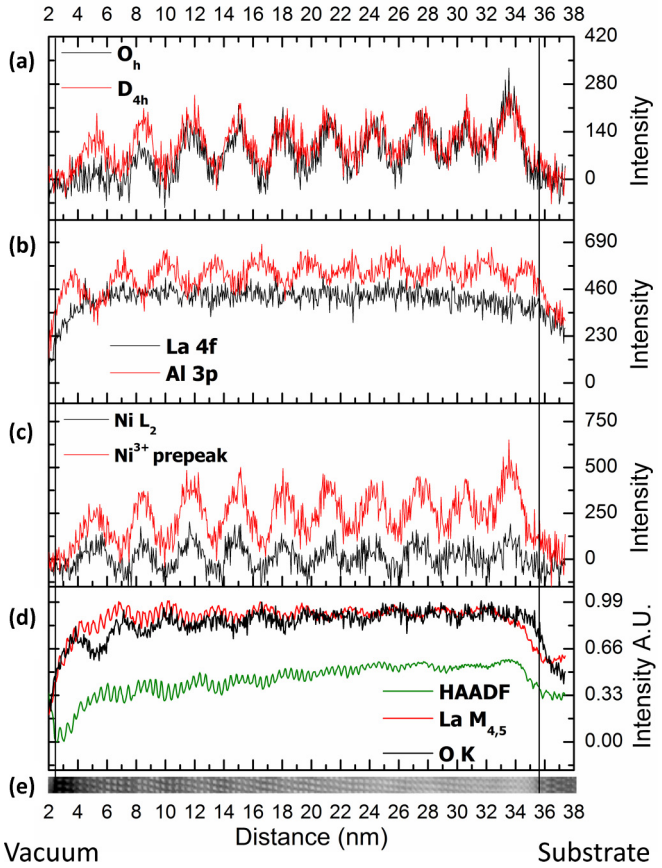

FIG. 7. (Color online) Line scans taken across a monochromated spectrum image integrated over the full spectrum image along the layers (perpendicular to the z direction) for (a) the two contributions of the Ni $3d$ prepeak [A: O_h (black) and B: D_{4h} (red)], (b) Ni L_2 (black) and the O K-edge prepeak A (red), (c) Al $3p$ (red) and La $5d$ (black) and the integrated signals of the full O K edge (black), La $M_{4,5}$ (red), and HAADF intensity (green) (normalized between 0 and 1) as well as the corresponding HAADF image (e). The drop in intensity close to the vacuum is due to the reduction of the sample thickness.

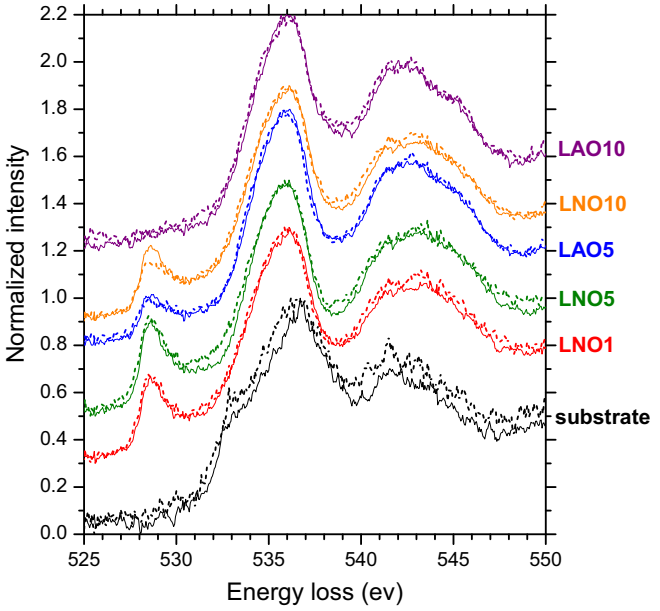

FIG. 8. (Color online) Monochromated spectra from the substrate, 3 LNO layers (LNO1, LNO5, and LNO10) and 2 LAO layers (LAO5 and the surface LAO layer) [named LNOX (LAOX) with X being the ordinal number of the LaNiO3 (LaAlO3) layer in the superlattice; 1 being the closest to the substrate] from two successive measurements in opposite scanning directions on the same area of the sample represented in plain (surface to substrate) and dashed lines (substrate to surface).

linked together as this prepeak in the LAO layer could be interpreted as an apparent "spilling" of Ni $3d$ hybridized states from the LNO layer into the LAO. Possible origins for such an intensity variation of the prepeak within the superlattice are (i) preparation or beam damage related oxygen loss, (ii) oxygen nonstoichiometry due to the growth conditions, (iii) interface roughness, and (iv) a change in hybridization due to heterostructuring, which we will discuss in detail in the following as these arguments allow us to understand the significant reduction of the prepeak intensity of the LNO layers present in the LNO/LAO heterostructure compared to the bulk stoichiometric phase LNO.

C. Possible origins of the O K-edge prepeak differences

(i) *Electron and ion beam damage*. We exclude a preparation-related oxygen loss based on the following arguments: the strongest argument follows from the comparison of our O K-edge EELS spectrum of the LNO thick film, which was grown, prepared, and measured under the same conditions (Fig. 4, spectrum d). This spectrum shows a Ni-O prepeak which is comparable in intensity, or even higher than in the reference data of Abbate *et al.* [32]. Further evidence is the excellent correspondence between the EELS spectrum obtained by integration of the signal of each pixel in the spectrum image [Fig. 5(a); 10 LAO + 10 LNO + a few atomic planes of the substrate] and the XAS data measured on the same film before preparation of the TEM sample, as seen from the comparison of curves f and g in Fig. 4. These two experimental spectra agree very well regarding the integrated intensity of the prepeak at 529 eV as well as in the region from 541 to 546 eV corresponding to the O $2p$–Ni $4sp$ transition. In order to rule out beam damage during the measurement, the same area was measured twice, from the substrate to the surface and from the surface to the substrate, and the results are identical (Fig. 8).

(ii) *Oxygen stoichiometry.* The reduced prepeak intensity might be related to a stoichiometry closer to $LaNiO_{2.75}$ than $LaNiO_{3.00}$ (Fig. 9), i.e., the presence of a non-negligible amount of Ni^{2+}, when growing LNO confined in a superlattice geometry. According to previous structural studies of $LaNiO_{3-\delta}$ in bulk [33,38] or thin-film form [39,40], a significant increase of 2%–5% of the pseudocubic unit-cell volume is expected when reducing $LaNiO_{3.00}$ to $LaNiO_{2.75}$. Accordingly, the unit-cell volume is, within our experimental error, equal or slightly smaller than the values for $LaNiO_{3.00}$ (see Appendix 2). Therefore, we exclude structural changes induced by oxygen vacancies. Within the accuracy of our method, we also found no evidence for oxygen

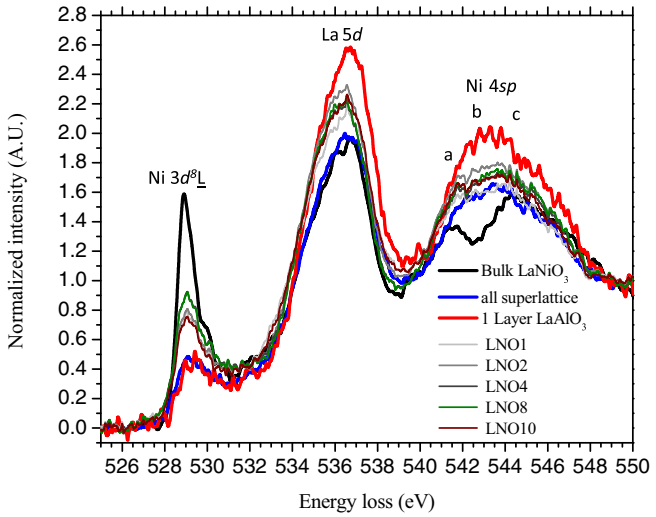

FIG. 9. (Color online) Comparison between the experimental raw monochromated EELS measurements averaged over the whole superstructure (blue), the reference $LaNiO_3$ sample (black), one layer of $LaAlO_3$ in the center of the superlattice (red), and some $LaNiO_3$ layers from the superlattice with their number (1 being the first layer close to the substrate and 10 the surface layer) in the same experimental conditions. Spectra are normalized to 1 in the region of energy between 548 and 550 eV and 0 before 527 eV.

nonstoichiometry from the quantitative analysis of the EELS data (see the Appendix 3 for details). Furthermore, the dc resistivity shown in Fig. 10 exhibits a metallic temperature dependence with $\rho(300\ \mathrm{K}) = 0.6\ \mathrm{m\Omega\,cm}$ for the superlattice and $\rho(300\ \mathrm{K}) = 0.4\ \mathrm{m\Omega\,cm}$ for the LNO film grown under the same conditions. The values are comparable to literature values reported for stoichiometric $LaNiO_3$ but much lower than values reported for $LaNiO_{3-\delta}$ [34,39,41,42]. In particular for $\delta = 0.25$, LNO exhibits a MI transition and for $\delta = 0.5$, the compound is insulating in the full temperature range considered here.

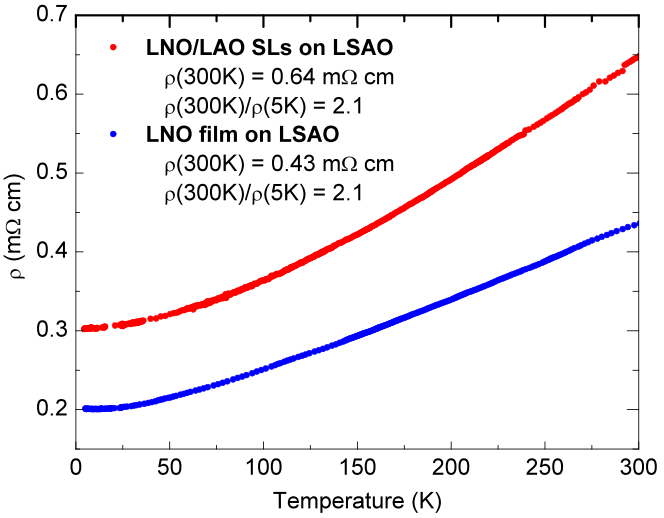

FIG. 10. (Color online) The dc resistivity of the studied LNO/LAO superlattice and the LNO film as a function of temperature measured in van der Pauw geometry.

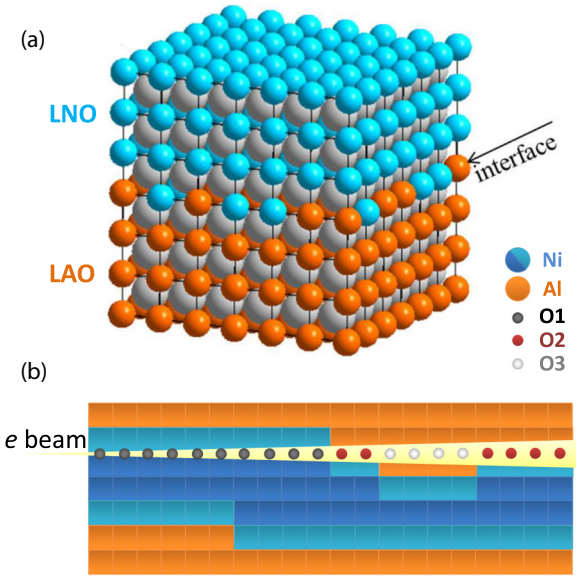

FIG. 11. (Color online) (a) Sketch of a LNO/LAO interface with ∼1 u.c. roughness. (b) Sketch of such an interface in a cut through the TEM lamella. Due to the roughness, the transmitted O K-edge EELS signal is a superposition of oxygen O1 which is bound to Ni ions only, of the interface oxygen O2 which is in a mixed Ni-O2-Al bond, and in the most extreme case also of O3 which is bound to Al only.

Regarding the electronic properties, an increased amount of Ni^{2+} at the LNO/LAO interfaces would result in an admixture of the $3d^8$ electron configuration which is not susceptible to orbital polarization since both e_g orbitals are occupied by a spin-up electron due to Hunds coupling (high-spin state). Therefore, a lower orbital polarization of the interface layers compared to the inner LNO layers in a 4-u.c.-thick layer stack is expected, opposite to the common trend some of us observed for LNO/LAO superlattices under compressive and tensile strain [23]. Furthermore, when reducing the LNO layer stack thickness from 4 to 2 u.c., a dimensionality-driven phase transition to an antiferromagnetic low-temperature phase which is accompanied by changes in the conductivity was observed [7,43]. This transition occurs irrespective of whether the substrate-induced strain is compressive or tensile and clearly distinguishes this transition from those in highly oxygen deficient $LaNiO_{3-\delta}$. Moreover, the reduced insulating phases require more than $\frac{1}{3}$ of divalent Ni^{2+}. Based on XRD, XAS, and hard x-ray photoemission data on our samples, we can clearly rule out such an amount of Ni^{2+}.

(iii) *Real and apparent roughness.* The LNO/LAO interface roughness of ∼1 u.c. might be important and would need to be taken into account since the measured signal is a spatial average over the TEM specimen thickness of 20 nm. Although the dynamical spread of our beam is only around 4 Å, i.e., 1 u.c. [15,25], it is likely that the measured signal is a mixture of signals arising from oxygen O1, which is bonded only to Ni ions, and oxygen O2, which is part of a Ni-O2-Al bond (see the sketch in Fig. 11). This implies a significant difference in Ni-O hybridization of the interface oxygen O2 which gives rise to a reduced Ni-O prepeak (in first approximation, the resulting

spectrum might be described by a weighted superposition of the LAO and LNO bulk spectra). This will be further discussed in point (iv) following. In addition, the tetragonal distortion induced by the substrate results in a slightly larger Ni/Al-O distance in the out-of-plane direction 1.931(3) Å compared to the averaged in-plane distances of 1.918(10) Å. Such an increased out-of-plane bond length may enhance the effect of reduced hybridization, in particular in the interface layers. This is supported by the observation that the intensity of the Ni L_2 profile reaches the baseline in each LAO layer, whereas the O $2p$–Ni $3d$ prepeak does not vanish when scanning across the O2 oxygen position since the Al-O2-Ni bonds connect the two materials. Taking the roughness into account the occurrence of the O $2p$–Ni $3d$ prepeak when scanning the inner LAO layers is also explained, as suggested above, by an apparent "spilling" of intensity of the O $2p$–Ni $3d$ hybridized states from the $LaNiO_3$ bulklike electronic structure into the LAO layer. In the topmost two layers of LAO, no Ni-O prepeak is observed, which we argue is due to the fact that those layers are surrounded by oxygen-depleted LNO layers. As discussed above, those vacancies are predominantly created at the apical position, i.e., include O2 vacancies, and therefore the prepeak is strongly suppressed.

In the following, we briefly address the impact of the interface roughness on the electronic properties reported so far [7,23,43]. Let us assume an interface roughness of 1 u.c. with LNO-LAO interface layers that are chemically mixed $La(Ni,Al)O_3$ [Fig. 11(a)] and further assume the extreme case of laterally alternating unit cells of LAO and LNO along this interface layer, i.e., each Ni atom is bound via oxygen to five Al neighbors and only to one Ni neighbor. If we now consider the nearest-neighbor hopping, this would yield a strong in-plane localization of Ni electrons since, these electrons, to first approximation can only delocalize in the direction perpendicular to the interface, along the Ni-O-Ni bonds pointing to the inner part of the LNO layer stack. For the orbital polarization ($P_{\text{interface}}$), this would result in a favored $3z^2 - r^2$ orbital occupation in the interface layers. For a less extreme lateral distribution of LNO and LAO unit cells in the interface layers, a more equal occupation of the e_g orbitals is expected, in agreement with our experimental result $P_{\text{interface}} = 0\%$ [23]. However, this would imply a scenario for tensile strain with $P_{\text{interface}} < P_{\text{inner-layers}}$, opposite to the experimental observation [23]. At first sight, the interface roughness alone may explain the localization observed in the conductivity of the 2//2 u.c. superlattices at lowest temperatures [7], but since the roughness does not change with temperature it is not in accordance with the observed temperature-dependent changes of the conductivity.

(iv) *Heterostructuring*. Finally, we discuss the change in hybridization due to heterostructuring. A reduced prepeak corresponds to a smaller hybridization of Ni and O compared to the bulk, i.e., LNO confined in a superlattice might be closer to a Ni $3d^7$ electron configuration than Ni $3d^8\underline{L}$ proposed for bulk $RNiO_3$ [16]. The absolute numbers of orbital polarization, as they have been defined and determined in Refs. [8,23], directly depend on the number of e_g electrons. The knowledge about the Ni ground-state electron configuration, i.e., how strongly Ni hybridizes with O, is of great interest for the theoretical understanding and treatment of $RNiO_3$ in general and LNO-based heterostructures in particular. A further understanding of the results presented in this work requires theoretical methods allowing an accurate calculation of the O K-edge spectra of correlated transition-metal oxides and the structural and chemical information provided by our work to refine the input parameters of the structure [44].

V. CONCLUSIONS

Using a combination of atomic EELS mapping and hybridization mapping of the oxygen K-edge fine structure, we were able to demonstrate the exact atomic arrangement of different types of interfaces occurring in a LNO/LAO superlattice grown on LSAO. First, the substrate-overlayer interface structure was determined to be La/SrO-La/SrO-AlO_2-LaO-$(Al,Ni)O_2$-LaO-NiO_2-LaO with the top LaO layer of the substrate being depleted of Sr ions. This implies a reconstruction of the area below the top layer of the substrate to the thermodynamically favored $LaAlO_3$ phase or diffusion of Al into the growing $LaNiO_3$ film. Further work is needed to discriminate these two scenarios. Second, the interfaces between LNO and LAO have been studied. The stoichiometry of the deeper buried LNO layers is very homogeneous. The O K-edge prepeak intensity is reduced compared to the LNO thin film grown under the same conditions. Possible origins, such as preparation or beam damage related oxygen loss, oxygen nonstoichiometry due to the growth conditions, interface roughness, and a change in hybridization due to heterostructuring, have been discussed. In conclusion, we demonstrated that hybridization mapping can add key information, including the change of crystallographic environment and stoichiometry in the understanding of interfaces in oxide heterostructures at the atomic scale. This powerful technique is now available due to recent developments (aberration correctors and monochromators) in TEM technology.

ACKNOWLEDGMENTS

We are thankful to J. Huang for FIB TEM sample preparation. G.A.B. gratefully acknowledges financial support from National Sciences and Engineering Research Council (NSERC), Canada (Discovery Grant Program). This work was supported by the German Science Foundation (DFG) and the Ministry of Science, Research and the Arts (MWK) of the state Baden-Württemberg within DFG:KA 1295/17-1 project and via TRR80, project G1. The experimental microscopy work was carried out at the Canadian Centre for Electron Microscopy (CCEM), a National Facility supported by NSERC and McMaster University. K. Meinander, A. Boris, and G. A. Sawatzky are gratefully acknowledged for fruitful discussions.

APPENDIX

1. Roughness from HAADF images

As can be seen on Figs. 12(a) and 12(b), the HAADF intensity provides some insight of the position of the interface between each stack in the superlattice and therefore it can be observed that layer thicknesses are in the range 2–6 unit cells, which means a roughness of ± 1 unit cell for each interface,

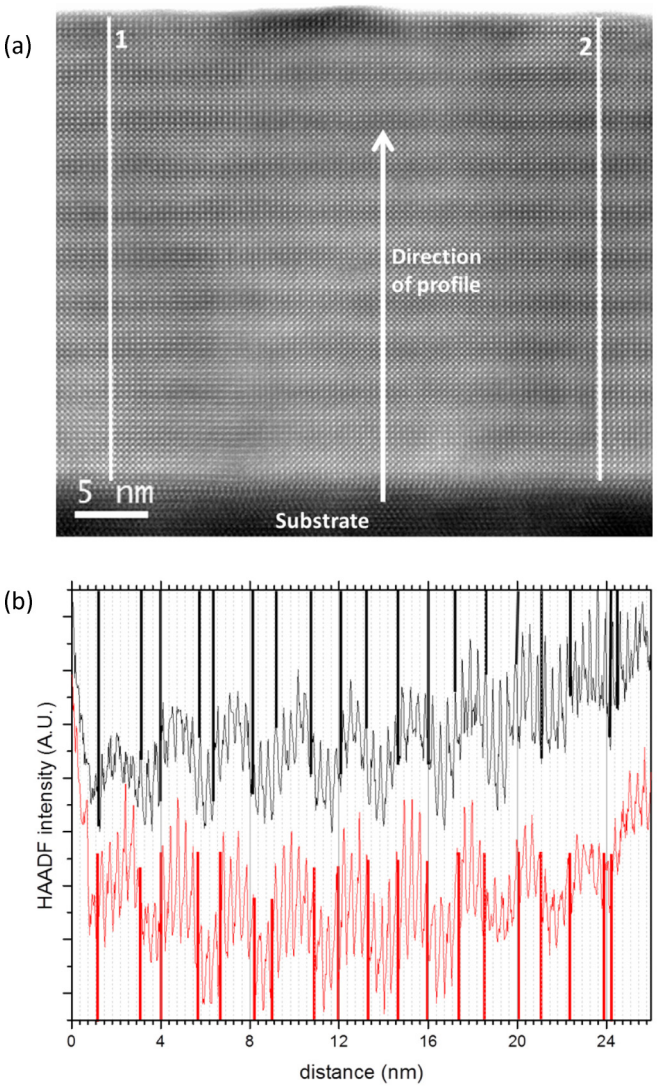

FIG. 12. (Color online) (a) HAADF image of the full superlattice viewed along the [100] direction. (b) Line profiles across the $(Ni,Al)O_2$ planes along lines 1 (black) and 2 (red) showing a rather constant roughness of ± 1 unit cell.

which is in good agreement with the global measurement by x-ray reflectivity [8,23].

2. Diffraction data analysis

From the analysis of our diffraction data we deduced pseudocubic (pc) lattice parameters $a = b = 3.75$ Å, and $c = 3.84$ Å for the averaged structure of the LNO and LAO layer stacks [23]. Due to the compressive strain induced by the substrate, the c parameter is slightly increased compared to the averaged bulk values of LNO and LAO ($a_{pc}^{LNO} = 3.838$ Å, $a_{pc}^{LAO} = 3.790$ Å$\rightarrow a_{average} = 3.814$ Å). Using $c_{LNO} = 2c_{SL} - c_{LAO}$ with $c_{LAO} = \frac{2\nu}{\nu-1}(a_{SL} - a_{LAO}^{bulk}) + a_{LAOO}^{bulk} = 3.816$ Å with $\nu = 0.26$ [45] and the lattice parameter reported in Ref. [23], we obtained an estimate of $c_{LNO} = 3.864$ Å for LNO in the superlattice (c_{SL} and a_{SL}, respectively, represent the lattice parameters along and perpendicular to the growth direction in the superlattice, and ν the Poisson ratio.

3. EELS quantification of oxygen content

Due to the strong overlap between the Ni L_3 and La M_4 white lines, a direct quantification based on ionization cross sections cannot be applied to determine the stoichiometry of the layers in the superlattice. Therefore, a standard-based quantification was performed as follows: An EELS spectrum was acquired over the full superlattice from 491 to 900.6 eV with a dispersion of 0.2 eV/pixel. The same measurement was performed over a reference sample (100-nm $LaNiO_3$ film on LSAO). After subtracting the background, the total intensity measured across the O K edge (from 526 to 551 eV) was integrated and named $I(O)$ hereafter. After subtracting the background in front of the La M_5 line, the total intensity of the La M_5 edge (from 821 to 838 eV) was integrated and named $I(La)$. This is done for spectra integrated over the two central unit cells for each of the layer stacks. The same analysis was performed for the full spectrum image taken from the reference sample, where the ratio of the number of oxygen atoms $N(O_{ref})$ to the number of La atoms $N(La_{ref})$ is known and equal to 3. The ratios $I(O)/I(La)$ were then calculated for each layer in the superlattice. From $I(O_{ref})/I(O_{ref})$, extracted in the same way for the reference sample, a correction factor K was calculated according to

$$\frac{N(O_{ref})}{N(La_{ref})} = K\frac{I(O_{ref})}{I(La_{ref})} = 3, \tag{A1}$$

where we deduce experimentally $K = 2.86$ and the stoichiometry of each layer stack (S) in the superlattice was then calculated using

$$S_i = \frac{I(O_i)}{I(La_i)}K. \tag{A2}$$

The error bars were estimated by the standard deviation of S_i, $\sigma(S_i)$, calculated with Eq. (A2) on each pixel of the spectrum image of the reference sample rebinned by 8 (giving n pixels) and subsequently on each layer and is equal to $\sigma(S_1, S_2, \ldots, S_n) = 0.12$, We can consider the confidence interval to be equal to 2σ corresponding to an error of 7% for the stoichiometry. All values of oxygen content obtained for both LAO and LNO layers are within this interval, showing the absence of a deviation of stoichiometry within the accuracy of the method.

[1] S. Lazar, Y. Shao, L. Gunawan, R. Nechache, A. Pignolet, and G. A. Botton, Microsc. Microanal. **16**, 416 (2010)
[2] N. Nakagawa, H. Y. Hwang, and D. A. Muller, Nat. Mater. **5**, 204 (2006).
[3] H. Y. Hwang, Y. Iwasa, M. Kawasaki, B. Keimer, N. Nagaosa, and Y. Tokura, Nat. Mater. **11**, 103 (2012).
[4] P. Zubko, S. Gariglio, M. Gabay, P. Ghosez, and J.-M. Triscone, Ann. Rev. Condens. Matter Phys. **2**, 141 (2011).

[5] M. Gibert, P. Zubko, R. Scherwitzl, J. Íñiguez, and J.-M. Triscone, Nat. Mater. **11**, 195 (2012).

[6] S. Wanchoo, J. Jasudasan, V. Bagwe, A. Thakur, U. Vaishnav, S. Pai, A. Narsale, and R. Pinto, Nucl. Instrum. Methods Phys. Res., Sect. B **212**, 539 (2003).

[7] A. V. Boris, Y. Matiks, E. Benckiser, A. Frano, P. Popovich, V. Hinkov, P. Wochner, M. Castro-Colin, E. Detemple, V. K. Malik, C. Bernhard, T. Prokscha, A. Suter, Z. Salman, E. Morenzoni, G. Cristiani, H.-U. Habermeier, and B. Keimer, Science **332**, 937 (2011).

[8] E. Benckiser, M. W. Haverkort, S. Brueck, E. Goering, S. Macke, A. Frano, X. Yang, O. K. Andersen, G. Cristiani, H.-U. Habermeier, A. V. Boris, I. Zegkinoglou, P. Wochner, H.-J. Kim, V. Hinkov, and B. Keimer, Nat. Mater. **10**, 189 (2011).

[9] J. Chakhalian, J. M. Rondinelli, J. Liu, B. A. Gray, M. Kareev, E. J. Moon, N. Prasai, J. L. Cohn, M. Varela, I. C. Tung, M. J. Bedzyk, S. G. Altendorf, F. Strigari, B. Dabrowski, L. H. Tjeng, P. J. Ryan, and J. W. Freeland, Phys. Rev. Lett. **107**, 116805 (2011).

[10] J. Chaloupka and G. Khaliullin, Phys. Rev. Lett. **100**, 016404 (2008).

[11] P. Hansmann, X. Yang, A. Toschi, G. Khaliullin, O. K. Andersen, and K. Held, Phys. Rev. Lett. **103**, 016401 (2009)

[12] P. Hansmann, A. Toschi, X. Yang, O. K. Andersen, and K. Held, Phys. Rev. B **82**, 235123 (2010).

[13] M. J. Han, C. A. Marianetti, and A. J. Millis, Phys. Rev. B **82**, 134408 (2010).

[14] C. Schüßler-Langeheine, J. Schlappa, A. Tanaka, Z. Hu, C. F. Chang, E. Schierle, M. Benomar, H. Ott, E. Weschke, G. Kaindl, O. Friedt, G. A. Sawatzky, H.-J. Lin, C. T. Chen, M. Braden, and L. H. Tjeng, Phys. Rev. Lett. **95**, 156402 (2005).

[15] N. Gauquelin, B. Gault, M. Bugnet, and G. A. Botton (unpublished).

[16] S. Johnston, A. Mukherjee, I. Elfimov, M. Berciu, and G. A. Sawatzky, Phys. Rev. Lett. **112**, 106404 (2014).

[17] X. Yang, P. Hansmann, A. Toschi, K. Held, G. Khaliullin, and O. K. Andersen (unpublished); see also O. K. Andersen, APS March Meeting (Pittsburgh, Pennsylvania, 2009).

[18] A. Blanca-Romero and R. Pentcheva, Phys. Rev. B **84**, 195450 (2011).

[19] M. J. Han, X. Wang, C. A. Marianetti, and A. J. Millis, Phys. Rev. Lett. **107**, 206804 (2011).

[20] M. J. Han and M. van Veenendaal, Phys. Rev. B **85**, 195102 (2012).

[21] N. Parragh, G. Sangiovanni, P. Hansmann, S. Hummel, K. Held, and A. Toschi, Phys. Rev. B **88**, 195116 (2013).

[22] J. W. Freeland, J. Liu, M. Kareev, B. Gray, J. W. Kim, P. Ryan, R. Pentcheva, and J. Chakhalian, Europhys. Lett. **96**, 57004 (2011).

[23] M. Wu, E. Benckiser, M. W. Haverkort, A. Frano, Y. Lu, U. Nwankwo, S. Brück, P. Audehm, E. Goering, S. Macke, V. Hinkov, P. Wochner, G. Christiani, S. Heinze, G. Logvenov, H.-U. Habermeier, and B. Keimer, Phys. Rev. B **88**, 125124 (2013).

[24] T. Malis, S. C. Cheng, and R. F. Egerton, J. Electron Microsc. Tech. **8**, 193 (1988).

[25] N. Gauquelin, D. G. Hawthorn, G. A. Sawatzky, R. Liang, D. A. Bonn, W. N. Hardy, and G. A. Botton, Nat. Commun. **5**, 4275 (2014).

[26] R. Egerton, *Electron Energy-Loss Spectroscopy in the Electron Microscope* (Springer, Boston, MA, 2011).

[27] M. Bosman, M. Watanabe, D. T. L. Alexander, and V. J. Keast, Ultramicroscopy **106**, 1024 (2006).

[28] C. Koch, Ph.D. thesis, Arizona State University, Phoenix, AZ, 2002.

[29] J. M. Rondinelli, S. J. May, and J. W. Freeland, MRS Bull. **37**, 261 (2012).

[30] A. Y. Dobin, K. R. Nikolaev, I. N. Krivorotov, R. M. Wentzcovitch, E. D. Dahlberg, and A. M. Goldman, Phys. Rev. B **68**, 113408 (2003).

[31] R. Egerton, Ultramicroscopy **107**, 575 (2007).

[32] M. Abbate, G. Zampieri, F. Prado, A. Caneiro, J. M. Gonzalez-Calbet, and M. Vallet-Regi, Phys. Rev. B **65**, 155101 (2002).

[33] M. Crespin, P. Levitz, and L. Gatineau, J. Chem. Soc., Faraday Trans. 2 **79**, 1181 (1983).

[34] R. D. Sánchez, M. T. Causa, A. Caneiro, A. Butera, M. Vallet-Regí, M. J. Sayagués, J. González-Calbet, F. García-Sanz, and J. Rivas, Phys. Rev. B **54**, 16574 (1996).

[35] P. Kuiper, J. van Elp, G. A. Sawatzky, A. Fujimori, S. Hosoya, and D. M. de Leeuw, Phys. Rev. B **44**, 4570 (1991).

[36] A. Becerra-Toledo and L. Marks, Surf. Sci. **604**, 1476 (2010).

[37] M. K. Kinyanjui, Y. Lu, N. Gauquelin, M. Wu, A. Frano, E. Benckiser, P. Wochner, G. Christiani, G. Logvenov, G. A. Botton, B. Keimer, and U. Kaiser, Appl. Phys. Lett. **104**, 221909 (2014).

[38] M. Crespin, O. Isnard, F. Dubois, J. Choisnet, and P. Odier, J. Solid State Chem. **178**, 1326 (2005).

[39] M. Kawai, S. Inoue, M. Mizumaki, N. Kawamura, N. Ichikawa, and Y. Shimakawa, Appl. Phys. Lett. **94**, 082102 (2009).

[40] B. Berini, N. Keller, B. Pigeau, Y. Dumont, E. Popova, N. Franco, and R. M. C. da Silva, J. Appl. Phys. **104**, 103539 (2008).

[41] J.-S. Zhou, J. B. Goodenough, B. Dabrowski, P. W. Klamut, and Z. Bukowski, Phys. Rev. B **61**, 4401 (2000).

[42] L. Qiao and X. Bi, Europhys. Lett. **93**, 57002 (2011).

[43] A. Frano, E. Schierle, M. W. Haverkort, Y. Lu, M. Wu, S. Blanco-Canosa, U. Nwankwo, A. V. Boris, P. Wochner, G. Cristiani, H. U. Habermeier, G. Logvenov, V. Hinkov, E. Benckiser, E. Weschke, and B. Keimer, Phys. Rev. Lett. **111**, 106804 (2013).

[44] Y. Lu, M. Höppner, O. Gunnarsson, and M. W. Haverkort, Phys. Rev. B **90**, 085102 (2014).

[45] X. Luo and B. Wang, J. Appl. Phys. **104**, 073518 (2008).